AIAA JOURNAL
Vol. 40, No. 7, July 2002

Time-Accurate Simulations and Acoustic Analysis of Slat Free Shear Layer

Mehdi R. Khorrami* and Bart A. Singer†
NASA Langley Research Center, Hampton, Virginia 23681-2199
and
Mert E. Berkman‡
High Technology Corporation, Hampton, Virginia 23666

A detailed computational aeroacoustic analysis of a high-lift flowfield is performed. Time-accurate Reynolds averaged Navier–Stokes computations simulate the free shear layer that originates from the slat cusp. Both unforced and forced cases are studied. Preliminary results show that the shear layer is a good amplifier of disturbances in the low- to midfrequency range. The Ffowcs Williams and Hawkings equation is solved to determine the acoustic field using the unsteady flow data from the Reynolds averaged Navier–Stokes calculations. The noise radiated from the excited shear layer has a spectral shape qualitatively similar to that obtained from measurements in a corresponding experimental study of the high-lift system.

Introduction

As part of a major effort to reduce aircraft noise emission, airframe noise has received renewed attention.[1] To develop viable noise reduction technologies, a concerted effort toward isolating and understanding noise sources associated with individual components of a high-lift system has been undertaken. Experimental studies by Hayes et al.,[2] Dobrzynski et al.,[3] Davy and Remy,[4] Grosche et al.,[5] Michel et al.,[6] Storms et al.,[7] and Olson et al.,[8] along with measurements at NASA Langley Research Center (LaRC), clearly show the importance of a leading-edge slat as a major contributor to overall airframe noise. The LaRC tests, which are the focus of our attention, involved a generic energy efficient transport (EET) high-lift model. The model comprises a slat, a main element, and a flap (Fig. 1). The model chord is approximately 10% of that of a Boeing 757. Both aerodynamic and acoustic measurements were obtained in the Low Turbulence Pressure Tunnel (LTPT) during entries in 1998 and 1999.

In the experiments, acoustic measurements were made by a team from Boeing Commercial Airplane Co. using the Boeing microphone-array technique. The array was mounted roughly 1 m from the underside of the model. The setting for the baseline case consisted of a main element angle of attack that varied between 6 and 10 deg, a flap deflection angle of 30 deg, and a slat deflection angle of 30 deg. For the angles of attack considered, the EET slat produces acoustic signatures that generally have similar features.

Representative microphone-array measurements for a 9-deg case from the 1999 entry are shown in Fig. 2. The plotted spectra are in $\frac{1}{12}$th-octave bands. The high-frequency microphone array had a smaller aperture than the low-frequency array and was better suited for resolving high-frequency noise. The flow Mach number is 0.2, corresponding to a typical approach condition. Two prominent features in the acoustic spectrum are a relatively high-amplitude peak near 50,000 Hz and high sound levels in the lower frequency range that drop abruptly between 4000 and 5000 Hz.

Previous efforts[9,10] proved our first conjecture that vortex shedding at the slat blunt trailing edge is the mechanism responsible for the tonal peak in the acoustic spectra at high frequencies. Those efforts focused on accurate unsteady Reynolds averaged Navier–Stokes (RANS) simulations of the slat trailing-edge flowfield and computation of the resulting acoustic far field. During the course of that study, our time-accurate RANS solution pointed to the presence of additional flow oscillations in the slat–cove region. The observed oscillations were associated with the slat free shear layer and had frequencies between 2000 and 4000 Hz. In the present paper, we extend our computational analysis of noise sources associated with a leading-edge slat in a high-lift setting. More precisely, current research applies the framework established in Refs. 9 and 10 to the free shear layer that originates at the slat cusp.

Early simulations[9] also suggested that the shear layer may self-excite and would not require explicit forcing. Therefore, our preliminary time-accurate simulations involved no forcing at the slat cusp, relying instead on the presence of numerical perturbations in the initial solution to provide the necessary excitation for the cove shear layer. Initially this natural forcing was adequate because the shear layer self-excited in the proper frequency band. Unfortunately, the excitation did not last more than a few periods before the shear layer instability modes were damped and the flowfield returned to its original quasi-steady state.

Lack of sustained disturbance growth prompted us to undertake a more thorough study. In this effort, we focused our attention on the role of large-scale instability modes of the slat shear layer in generating noise. Therefore, goals of the present study are to test our conjecture that amplified perturbations in the free shear layer are responsible for low-frequency content of the acoustic spectra. Although similar conjectures have been put forth by other investigators,[3] the issue remains unresolved. Although our current simulations were started in late 1998 and early 1999, two recent studies lend added support to our conjecture. Using particle image velocimetry (PIV), Paschal et al.[11] were able to map the flowfield slightly downstream of the slat trailing edge. At low angles of attack (4 deg), the PIV-generated images show the presence of large, strong spanwise vortices in the slat's wake. Size and location of these rollers, relative to the wake, preclude the slat trailing edge as the source. In all likelihood, as pointed out by Paschal et al., these vortices originate from the slat–cove region and then

---

Received 19 May 2001; presented as Paper 2001-2155 at the AIAA/CEAS 7th Aeroacoustics Conference, Maastricht, The Netherlands, 28–30 May 2001; revision received 20 January 2002; accepted for publication 24 January 2002.

*Research Scientist, Computational Modeling and Simulation Branch. Associate Fellow AIAA.

†Assistant Branch Head, Computational Modeling and Simulation Branch. Senior Member AIAA.

‡Research Scientist; currently Senior Project Engineer, Air and Emissions Technologies, ArvinMeritor, Inc., 950 W. 450 S, Building 2, Columbus, IN 47201.

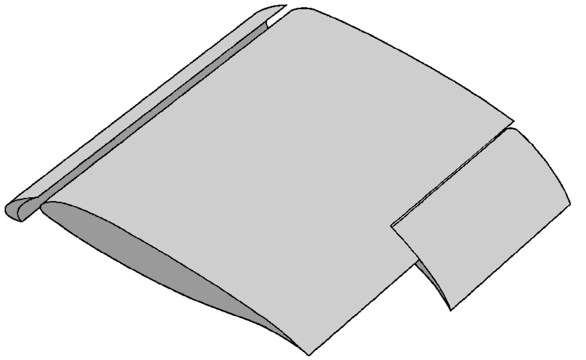

a) Three-dimensional model

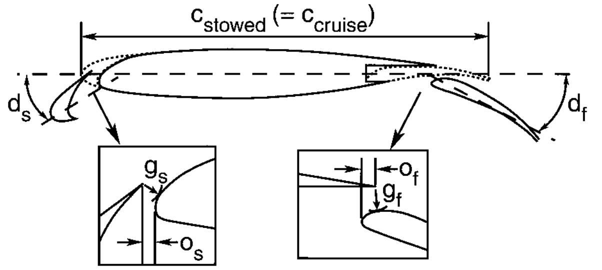

b) Cross-sectional view

Fig. 1 Three-element EET high-lift system with $C_{\mathrm{stowed}} = 0.55$ m.

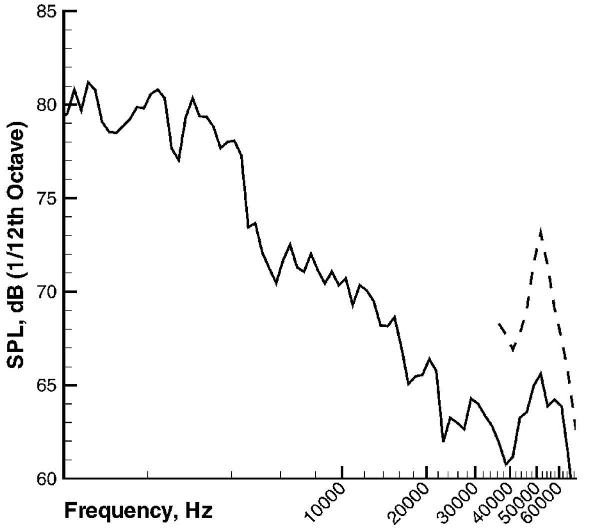

Fig. 2 Measured acoustic spectrum for slat in 1/12th-octave bands; test parameters are slat deflection angle 30 deg, main element angle of attack 9 deg, flap deflection angle 30 deg, Mach number 0.2, and Reynolds number of 7.5 × 10^6: ——, low-frequency microphone array and - - -, high-frequency microphone array.

are pumped through the gap. As the angle of attack is increased, unsteadiness coming out of the cove is diminished, and the number of vortices in the wake is reduced significantly. Similarly, Takeda et al.[12] employed the PIV technique to map the flowfield inside a slat–cove area. Growth of the shear layer disturbances and their subsequent evolution into large-scale structures were captured.

Computational Approach

The computational framework employed in the present study was explained in detail in Refs. 9 and 10. Only a brief overview is given here.

As in Ref. 9, the CFL3D solver is used to perform time-accurate flowfield simulations. CFL3D is a finite volume formulation-based code that solves time-dependent compressible thin-layer Navier–Stokes equations. CFL3D offers a wide variety of turbulence models, including zero-, one-, and two-equation models. Based on our past experience, the two-equation Shear Stress Transport (SST) (k–ω) Menter[13] model is selected and preferred for the present problem.

All current computations are performed using effectively second-order-accurate time discretization and the dual time-stepping method.[14] In conjunction with three-level V-type multigrid cycles, 30 subiterations are utilized to ensure approximately two orders of magnitude drop in both mean flow and turbulence-model residuals during each time step.

High-Lift Configuration

A full account of the three-element high-lift EET model and grid construction has been given by Khorrami et al.[9] For the present work, it suffices to mention that, in the stowed position, the model has a chord of 21.65 in. (0.55 m) with slat and flap chords of 15 and 30%, respectively. The geometrical settings associated with the slat and flap (gaps g_s and g_f and overhangs o_s and o_f) in the baseline experiment are provided in Table 1, where the distances are given as a percentage of the stowed chord. A graphical representation of the respective gaps and overhangs is shown in Fig. 1b. In the 1998 entry, angle of attack for the baseline experiment was set at 10 deg, and the deployed flap was part span. To match loading on the slat and the main element, the present two-dimensional simulations are performed at 8-deg angle of attack. In the 1999 entry, the part-span flap was replaced by a full-span flap with a slightly different profile. The slat gap and overhang remained identical. The new flap had little effect on relevant features of the measured acoustic spectra. Therefore, current simulations, which are conducted using the original flap profile, apply to both 1998 and 1999 experiments.

The present grid is identical to the refined grid employed in Ref. 9. The two-dimensional grid has 21 blocks and approximately 433,000 total nodes. More than 60% of the points are clustered in regions surrounding the slat and leading edge of the main element.

Forcing Strategy

As discussed in the Introduction and based on our previous simulations, a decision was made to introduce low levels of forcing into the flowfield. Controlled forcing helps to isolate and capture the mechanism(s) responsible for low-frequency oscillations observed in the slat–cove region. The forcing location was selected roughly two to three local boundary layer heights upstream of the finite thickness cusp (Fig. 3). The small but finite distance between the forcing location and the cusp minimized dissipation of the disturbances before the separation at the cusp, but allowed the forcing to be distributed over a small region, thereby reducing anomalous effects that might be caused by single-point forcing at the cusp. The forced quantity is the vertical velocity, which at the forcing

Table 1 Geometrical settings

High-lift parameter	Value
Slat angle δ_s	30 deg
Flap angle δ_f	30 deg
Slat gap g_s	2.44%
Flap gap g_f	3.0%
Slat overhang o_s	−1.52%
Flap overhang o_f	1.7%

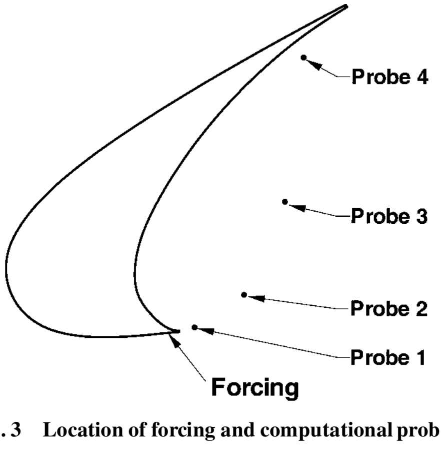

Fig. 3 Location of forcing and computational probes.

location, closely approximates the wall-normal velocity. A simple harmonic function given by Eqs. (1) and (2) was chosen to represent the forcing function, where t and x denote time and distance in the streamwise direction, respectively:

$$g(x,t) = \frac{A_0}{\sqrt{N}} h(x) \sum_{i=1}^{N} \sin(\Omega_i t + \psi_i) \tag{1}$$

$$h(x) = 1 - b_1(x - b_2)^2 \tag{2}$$

In Eq. (1), the summation is over N equally spaced frequency bins, each with a center frequency Ω_i that differs by 93 Hz. The specific value of 93 Hz was chosen based on N and the selected frequency range of interest. No other frequency bin sizes were tried. To ensure the independence of individual frequencies, a randomly generated phase ψ_i is assigned to each frequency. Also note that, to avoid forcing at a single point, the amplitude of the source is distributed over several grid nodes (seven in the present case) using a parabolic variation in x. The constants b_1 and b_2 are chosen to ensure zero velocity at the edges of the forcing region. Finally, A_0 represents the rms of the signal and is used to set desired amplitude levels.

The time-consuming nature of the unsteady simulations and the need to generate meaningful time records limited the number of cases computed. The present set of computations focuses on flowfields forced over two different frequency bands. The first simulation involves a frequency band $1200 < f < 5000$ Hz, corresponding to the observed range of frequencies of interest in the measured spectra. Once it became clear (from the simulated flowfield) that the shear layer is an efficient amplifier of disturbances in the observed frequency range, the frequency of the forcing function was expanded to encompass a range approximately twice that of the initial distribution. For the second simulation, the selected frequency band is $700 < f < 10{,}000$ Hz. Widening the frequency band was significant for two related reasons. Given the shear layer's thinness near the cusp, a wider frequency band allows a more natural selection process for the most amplified disturbances. In addition, it removes any ambiguity regarding the effect of initial forcing distribution on the final outcome of the established flowfield. Although our initial amplitude levels of 0.5 and 1.0% (of the freestream velocity) did produce shear layer undulation in the correct frequency band, the unsteadiness levels were very weak and the growing disturbances remained in the linear regime. Therefore, for both frequency ranges, the rms amplitude A_0 is fixed at 3% of the freestream velocity.

Acoustic Procedure

Previously, Singer et al.[10,15] explored the use of unsteady computational results in acoustic-propagation codes based on the Ffowcs Williams and Hawkings[16] (FW–H) equation. Such codes compute the acoustic signal at a distant observer position by integrating the FW–H equation. Following Brentner and Farassat,[17] the FW–H equation may be written in differential form as

$$\Box^2 p'(x,t) = \frac{\partial^2}{\partial x_i \partial x_j}[T_{ij} H(f)] - \frac{\partial}{\partial x_i}[L_i \delta(f)] + \frac{\partial}{\partial t}[(\rho_0 U_n)\delta(f)] \tag{3}$$

where

$$\Box^2 \equiv \frac{1}{c^2}\frac{\partial^2}{\partial t^2} - \nabla^2$$

is the wave operator, c is ambient speed of sound, t is observer time, p' is acoustic pressure, ρ_0 is freestream density, $f = 0$ describes the data surface, $\delta(f)$ is the Dirac delta function, and $H(f)$ is the Heaviside function. The quantities U_i and L_i are defined as

$$U_i = (1 - \rho/\rho_0)v_i + \rho u_i/\rho_0 \tag{4}$$

$$L_i = P_{ij}\hat{n}_j + \rho u_i(u_n - v_n) \tag{5}$$

respectively. In Eqs. (4) and (5), ρ is total density, ρu_i is momentum in the i direction, v_i is velocity of the data surface $f = 0$, and P_{ij} is the compressive stress tensor. For an inviscid fluid, $P_{ij} = p\delta_{ij}$, where p is the perturbation pressure and δ_{ij} is the Kronecker delta. The subscript n indicates projection of a vector quantity in the surface-normal direction. To obtain a solution to Eq. (3), the first term on the right-hand side must be integrated over the volume outside the data surface $f = 0$ wherever the Lighthill stress tensor T_{ij} is nonzero in this region. In the work reported here, this term is neglected; however, the main effects of nonzero T_{ij} within the flow can be included by choosing a data surface containing all of the volume with significant T_{ij} contributions. Therefore, the data surface defined by $f = 0$ is a surface within which all of the important noise sources are assumed to be located. In such a situation, only flow data on the surface $f = 0$ are required in the solution of the FW–H equation.

The other terms on the right-hand side of Eq. (3) include those determined by the unsteady flowfield on the data surface. Provided that the unsteady flow on data surface $f = 0$ is correct, in Ref. 15 it is demonstrated that the FW–H equation correctly propagates the acoustic radiation from several source regions, including complex signals associated with acoustic scattering from sharp edges. In Ref. 10, it is demonstrated that use of the FW–H equation propagates noise generated at the trailing edge of a slat.

Here only the two-dimensional version of the FW–H equation is used to predict the sound field. We use an extremely efficient code developed by Lockard[18] for computing the two-dimensional acoustic field from two-dimensional computational fluid dynamics (CFD) data. The code performs the computation in the frequency domain; hence, unsteady CFD data must be transformed from the time domain.

Transformation involves first removing initial transient data from the CFD calculation. Then, the data record is divided into segments of 4096 time steps with the latter 2048 time steps of each record being incorporated into the subsequent segment. A modified Hanning window is applied to each data segment. The modified Hanning window includes a standard Hanning filter for the first and last 12.5% of the data and a boxcar filter for the middle 75%. Windowed data are scaled to preserve the original energy in the signal and then Fourier transformed into the frequency domain. The data segments introduce an artificial periodicity of 366 Hz, but this frequency is far lower than the frequencies of interest in this flow. The spectra obtained with each of the 4096 time steps are then averaged to smooth the spectrum.

All acoustic calculations are performed for observers located a fixed distance from the slat's trailing edge. The fixed distance corresponds closely to the distance from the slat trailing edge to the wind-tunnel ceiling. Directivity angles are indicated in Fig. 4: 0 deg is in the downstream direction and 270 deg is groundward in normal flight, but toward the microphone array in the wind tunnel.

Figure 5 shows the upstream portion of data surfaces used for the FW–H calculations reported here. Figure 5a shows the upstream portion of the on-body data surface. This data surface is coincident with the slat and main element bodies. Figure 5b shows the

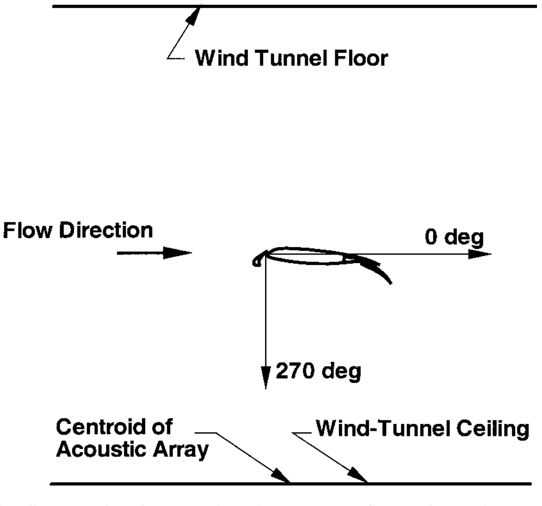

Fig. 4 Schematic of model in wind tunnel, flow left to right, acoustic directivity angles 0 and 270 deg indicated; view rotated relative to experimental setup.

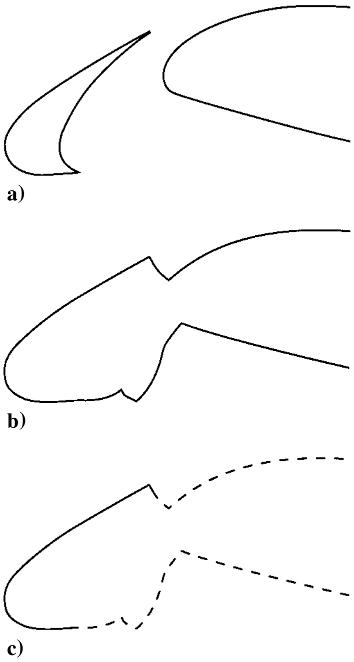

Fig. 5 Data surfaces used for FW–H calculations: a) on-body data surface, b) standard off-body data surface, and c) modified off-body data surface (– – – section is same as standard off-body data surface; —— section is same as on-body data surface).

upstream portion of the standard off-body data surface. This data surface extends outside the boundary layer of high-lift elements and encompasses the slat–cove region. Figure 5c shows a modified off-body data surface. The modified off-body data surface is the same as the standard off-body data surface over the dashed-line region; however, over the solid-line region (essentially the slat's suction surface), the modified off-body data surface uses the on-body grid and data. Reasons for use of the modified data surface will be discussed later.

Results

RANS Simulations

Computations and postprocessing of the results are carried out in a nondimensional fashion. The nondimensionalization is with respect to a reference length (stowed chord), a reference speed of sound a_∞, a reference density ρ_∞, and a reference kinematic viscosity ν_∞. For the present case, reference flow variables were set to match conditions at the LTPT test section entrance. Computations are done in a fully turbulent mode using the two-equation SST k–ω turbulence model. Unless indicated otherwise, all simulations are obtained for $M = 0.2$ and $Re = 7.2 \times 10^6$.

The initial simulation was started in the steady mode to deduce the accuracy and grid dependency of the numerical results. During the mesh sequencing step, the midlevel mesh (with every other grid point removed) and the fine-level mesh produced lift coefficients of 3.13 and 3.07, respectively, resulting in a difference of less than 2%. The difference between the drag coefficients came out to be slightly larger and close to 5%.

A constant nondimensional time step of $\Delta t = 4.116 \times 10^{-4}$ (corresponding to 200 points per period for a 7500-Hz signal) is used for all time-accurate simulations. The current Δt is four times larger than the time step used in Ref. 9. We chose a larger Δt to strike a balance between temporal resolution required for high-frequency trailing-edge vortex shedding and the need to generate a sufficiently long record to search for low-frequency shear layer instabilities. When the larger time step was used, the frequency and amplitude of the high-frequency trailing-edge shedding remained substantially the same as with the smaller time step; hence the temporal resolution for the lower frequency disturbances that were the focus of this work should also be adequately time resolved.

Figures 6a–6c show the instantaneous spanwise vorticity field in the slat vicinity for the forced case with the smaller frequency band. The three snapshots are sequential in time, with $1024\Delta t$ and $1408\Delta t$ separating the second frame from the first, and the third frame from the second, respectively. To put these separation times in perspective, using the freestream velocity, the approximate convective travel time from cusp to trailing edge is about $1400\Delta t$. In Fig. 6, the most notable features in each snapshot are the formation of a free shear layer due to boundary-layer separation at the slat cusp and the presence of a strong vortex shedding at the blunt trailing edge. Vorticity contours clearly display the spatial location of

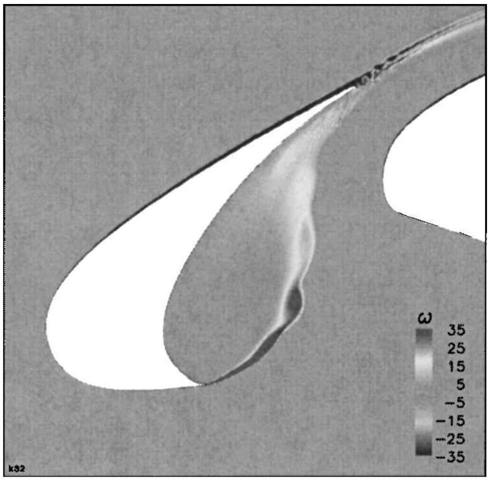

a) Early time

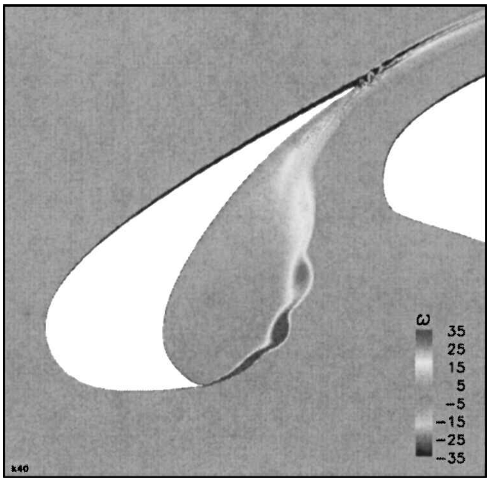

b) Middle time

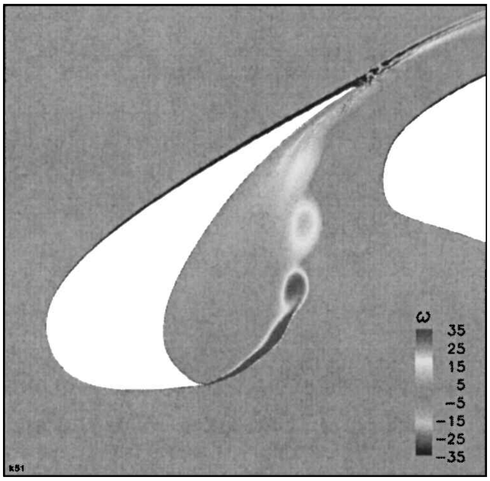

c) Later time

Fig. 6 Simulated spanwise vorticity field for narrow bandwidth 3% forced case.

the free shear layer. Also the time evolution of the slat's shear layer is vividly apparent. Notice that the shear layer is a good amplifier of initial perturbations that result in a shear layer rollup process and the formation of discrete vortices. Amplification of disturbances occurs via the well known Kelvin–Helmholtz (inflectional) instability mechanism.

Once formed, the vortices convect upward and impinge on the slat undersurface at the reattachment point. When the reattachment point is approached, the vortices experience severe stretching and distortion due to rapid deceleration and subsequent acceleration of the local flowfield. Vorticity plots also indicate that the large-scale structures disappear before reaching the slat trailing edge, and no lumps of vorticity resembling a vortex escape through the gap.

Time-accurate simulation with the narrowband ($1200 < f < 5000$ Hz) excitation confirmed our suspicions regarding the shear layer supporting large-scale unsteady structures. Therefore, starting from the same initial base flow, the computation was repeated for the wider excitation band of $700 < f < 10{,}000$ Hz. Both simulations, with the exception of minor details, produce flowfields with similar features. Figures 7a and 7b provide a sample comparison between the computed spanwise vorticity field at the same instant in time. The shear layer rollup location and the size of the rollers are virtually the same, indicating nearly identical frequencies for the most amplified disturbances. Given the nearly identical states of the disturbed shear layer, for the remainder of this section only the computation obtained with the wider forcing band will be presented.

To determine shear layer dominant modes of oscillation, several computational probes are placed within the computational domain in the slat's vicinity. We use the term computational probe here to signify the act of collecting time-dependent variables at a single point in the computation. Locations of the four primary probes used to ascertain time evolution of the shear layer are shown in Fig. 3. Probe 1 is closest to the slat cusp, whereas probe 4 is situated near the shear layer reattachment point. A sample record obtained from probe 3 inside the shear layer is plotted in Fig. 8. The prominent high-frequency oscillations are due to strong vortex shedding at the slat trailing edge. Each period in this frequency range includes about 35 time steps. The high-frequency signal is superimposed on much lower frequency oscillations caused by shear-layer instability. Based on the Fourier transform of the recorded time signals, the shear layer primary mode has a frequency that resides between 2000 and 3000 Hz.

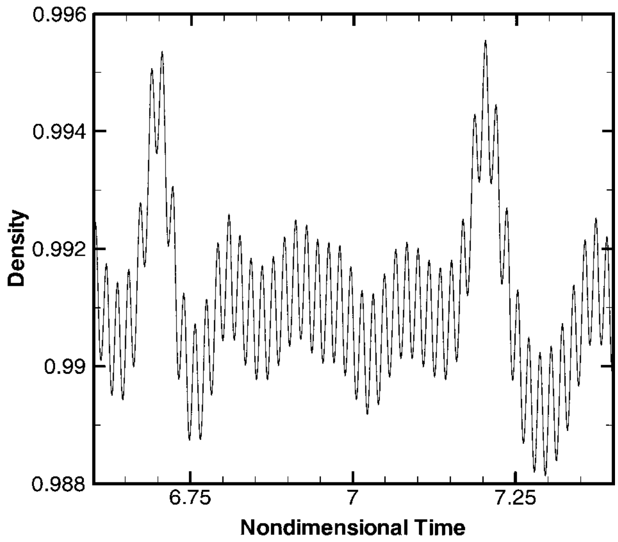

Fig. 8 Sample time record from computational probe 3.

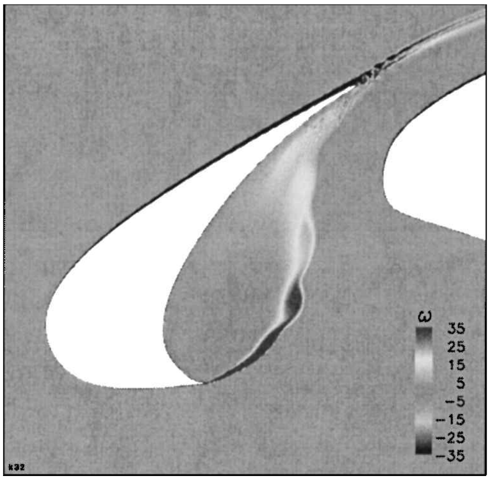

a) Narrowband excitation

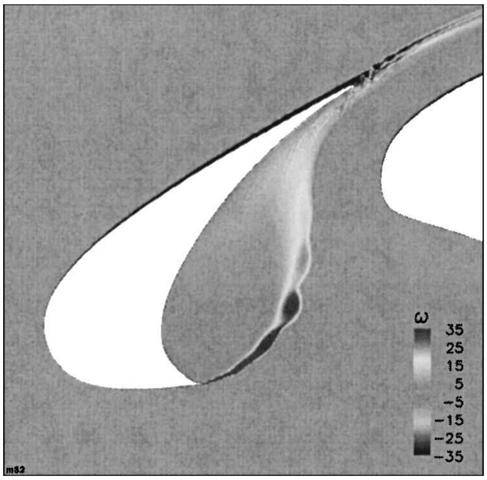

b) Wideband excitation

Fig. 7 Comparison between spanwise vorticity fields.

Contrary to what one might expect, the recorded data do not indicate a continuous rollup process that results in the formation of a vortex chain; rather, they show the process to be somewhat intermittent. For example, the time signal in Fig. 8 shows the passage of a large-scale structure close to $t = 6.7$, followed by a period of relatively lower amplitude oscillations followed by the passage of another vortex at $t = 7.2$. Scrutiny of the entire recorded signal in conjunction with the corresponding vorticity field failed to reveal a discernible pattern of a particular periodicity. At times, five or six vortices in a row are produced by the rolling up of the shear layer followed by a period of low activity, whereas at other times, only one or two vortices are formed. However, even during low-activity periods, low-frequency disturbances are still being amplified, producing weak undulations of the shear layer. Most likely, during these weak undulations the disturbances experience and undergo a linear growth stage without reaching the latter stages of nonlinear growth and saturation states. To better understand the relation between this intermittent behavior and the external forcing, correlations of the forcing function with signals from the four probes were calculated. The highest attainable correlation produced a value close to 0.3, suggesting only a weak correlation. As expected, the closer probes to the slat cusp provided the higher correlations.

To present a more complete physical picture of disturbance evolution along the shear layer, unsteady signals from the four probes are considered simultaneously. Figure 9 shows the four individual time records Fourier transformed. Jaggedness of the transformed signals is due to the combination of 1) the finiteness of the record and 2) the discreteness of the forced frequencies. Near the cusp (probe 1), the shear layer is thin and, thus, supports a wider frequency band of instabilities. Accordingly, we expect the fastest growing modes to have relatively high frequencies. The transformed signal from probe 1 supports this claim and shows the most amplified disturbances are confined to the range $5000 < f < 10{,}000$ Hz. As the shear layer thickens downstream, the band of disturbances with the highest growth rates gradually shifts toward lower frequencies. Plotted signals from probes 2 and 3 clearly confirm this slow shifting of

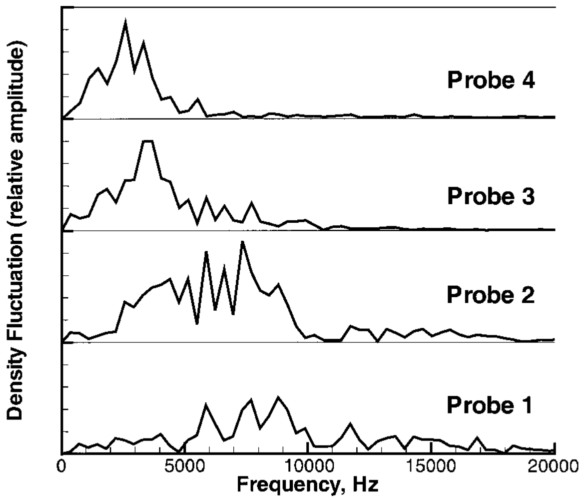

Fig. 9 Fourier transforms of computational probe data.

the amplified frequency band. By the time the shear layer reattachment location (probe 4) is reached, high-frequency perturbations are damped, and energy is concentrated in the frequency band of $1000 < f < 4000$ Hz. The upper limit of 4000 Hz agrees favorably with the slat's acoustic spectrum frequencies (Fig. 2), where amplitude drops off very rapidly. This agreement reinforces our opinion that flow unsteadiness supported by the shear layer is the mechanism responsible for the low-frequency content of the slat acoustic spectrum.

Based on current and other recent studies, one may argue that an unsteady RANS simulation provides a useful tool for understanding complex flow-generated noise sources. Yet, as in the case of any computational methodology, some inherent deficiencies deserve our comments before concluding the section. For the present set of simulations, a point of concern is the rapid dissipation of a rolled-up vortex (see Fig. 6c). In the present simulations, a typical roller is resolved with over 20 points along the stream and more than 40 points in the normal directions. Thus, our spatial resolution of the cove region is fine enough to discard numerical viscosity as a major contributor. We believe the only other factor with such first-order dissipative effects is the turbulence model. Most general purpose turbulence models are developed and calibrated for wall-bounded steady flowfields. The behavior of these models in an unsteady free shear flow is uncertain. We must reiterate, however, that our focus has been to uncover and highlight mechanisms responsible for slat noise. Issues concerning the turbulence model effects are beyond the scope of the present effort and deserve a thorough study of their own.

Acoustic Analysis

Figure 10 shows a directivity plot for the case in which a 3% wideband forcing was applied. Only the energy in frequencies between 1000 and 20,000 Hz was used in computing directivity displayed here. The standard off-body data surface was used for the calculation. Noise preferentially propagates forward and downward, but the directivity plot does not contain significant strongly directed lobes. Lack of strongly directed lobes is consistent with the broadband nature of the noise. Directivity plots that include narrower ranges of frequencies show more pronounced directivity sensitivity, mostly in the downstream direction (0 deg). Because of the importance of the flyover direction (270 deg) and because the directivity in the vicinity of 270 deg is not particularly sensitive to small changes in angle, all spectra reported here are taken at 270 deg.

Figure 11 shows a comparison of the acoustic spectra obtained at 270 deg for two cases. In the first case, a 3% forcing was applied in a frequency band $1200 < f < 5000$ Hz (solid line). In the second case, a 3% forcing was applied in a frequency band $700 < f < 10{,}000$ Hz (dashed line). For the first case, after the transient was removed, spectra from two data segments were averaged to obtain the result shown. In the second case, spectra from four data segments were averaged. More data averaging would be desirable in both cases; however, even with the marginal data averaging, in both cases the sound pressure level (SPL) decreases significantly in the vicinity of respective maximum forcing frequencies. Strong decreases at these frequencies suggest that the sound radiated is strongly correlated to details of the forcing. The spectra associated with the flow structures themselves (Fig. 9) do not contain particularly sharp cutoffs at the lower and upper excitation frequencies. For the acoustic data to be useful, we needed to understand why the acoustic field was more sensitive to forcing than the flowfield.

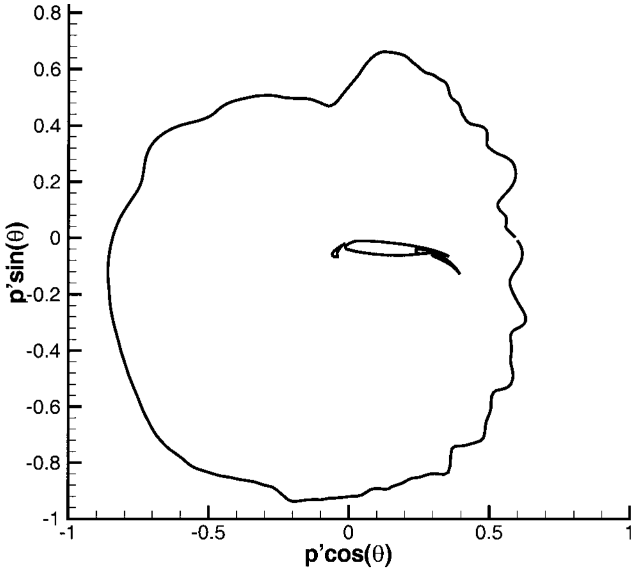

Fig. 10 Far-field noise directivity pattern.

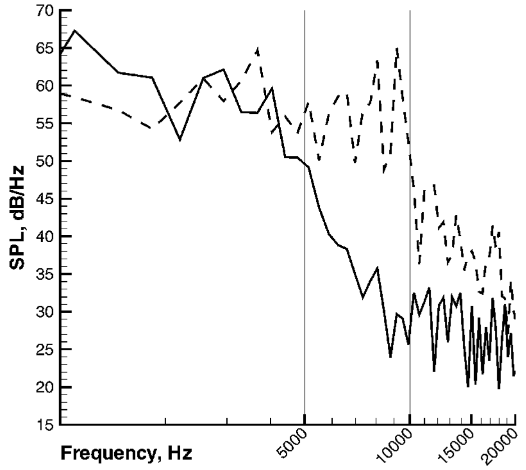

Fig. 11 Far-field noise spectra at 270 deg for 3% forced cases: ——, forcing $1200 < f < 5000$ Hz and - - -, forcing $700 < f < 10{,}000$ Hz; vertical lines mark 5000 and 10,000 Hz, and reference pressure is 20 μPa.

One possibility for stronger sensitivity of the acoustics to forcing is that acoustic radiation might be dominated by acoustic scattering at the slat cusp. Because the slat cusp is only a small distance downstream of the forcing location, the effect of forcing might be expected to be higher right at the cusp than in the unstable shear layer. If acoustic scattering at the slat cusp was the reason for strong sensitivity in the acoustics to forcing, then use of the on-body data surface in the FW–H solver would give similar results to those obtained using the standard off-body data surface. In particular, the strong decrease in SPL around the maximum forcing frequency would be expected in both cases. Figure 12 shows a comparison of the spectra at 270 deg using the on-body data surface (solid line) and the standard off-body data surface (dashed line). In these calculations, flow velocity relative to the on-body data surface is assumed zero. Figure 12 shows that the SPL starts to drop at a significantly lower frequency for the case in which the on-body data surface is

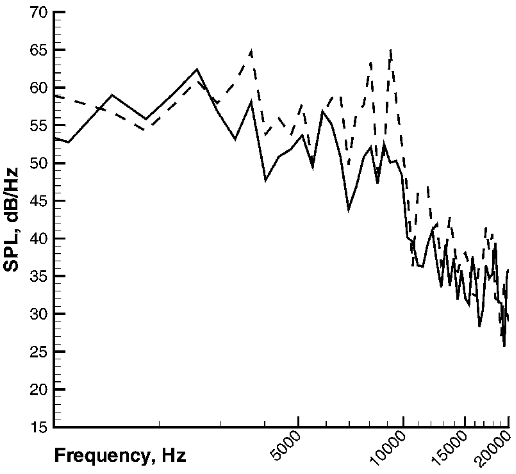

Fig. 12 Far-field noise spectra at 270 deg for 3% forcing $700 < f < 10{,}000$ Hz: ——, on-body data surface and - - -, standard off-body data surface, with reference pressure 20 μPa.

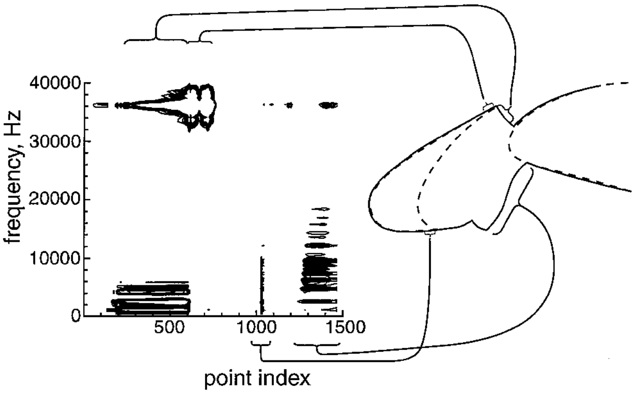

Fig. 13 Contours of forcing term U_n as function of frequency and point position.

used. A similar conclusion is reached for comparisons with the case in which forcing was stopped at 5000 Hz. Acoustic scattering at the slat cusp was thereby ruled out as the source of the strong correlation between forcing and the acoustic spectrum.

Another set of FW–H calculations was performed with a data surface slightly dissimilar to the on-body data surface. Rather than being on the slat surface, the surface on the suction side of the slat was replaced by a surface that was just outside of the slat boundary layer. This very small displacement of the surface to outside the boundary layer was not expected to influence the acoustic results much. Surprisingly, the acoustic spectrum for this case was more similar to that obtained with the standard off-body data surface than with the on-body data surface.

The unpredicted behavior led to a desire to identify regions in which the right-hand side of the FW–H equation [Eq. (3)] was large. These would be the regions that would dominate the far-field radiation. Figure 13 includes contours of U_n from Eq. (3) in a point-index-frequency plane. The schematic in Fig. 13 shows the slat and main element bodies with dashed lines and the standard off-body data surface with a solid line. Leader lines show the correspondence of the various point indices to their locations on the off-body data surface. Although Fig. 13 only shows data for the case in which 3% forcing was applied between 700 and 10,000 Hz, the conclusions also apply to the case in which forcing was applied between 1200 and 5000 Hz.

The source term U_n is large in the 35,000–38,000-Hz range, and vortex shedding at the slat's trailing edge dominates the source term at these high frequencies. This phenomenon and its acoustic implications are reported in Refs. 9 and 10. The source term U_n is also very strong in the 2000–3000-Hz range in the gap between the slat trailing edge and the main element. This large value is the result of acoustic radiation through the slat gap. This noise is most likely generated by flow structures associated with the shear layer instabilities, probably as the flow structures interact with the slat.

Two other regions also show large values of U_n; both regions show that the source term is strong up to 10,000 Hz. One of these regions is a portion of the off-body surface stretching over a section of the cove. The other region is tightly clustered around the location at which forcing is applied. In retrospect, the U_n term should be large in the vicinity of the forcing. Forcing is applied as an oscillating mass flux through a small section of the slat. The oscillating mass flux directly contributes to source terms on the right-hand side of Eq. (3). The forcing is itself an acoustic source, and direct radiation of that acoustic energy must be properly handled by the data surface. When diffraction effects are neglected, direct radiation of acoustic energy from forcing is expected to be most apparent on surfaces within a line of sight of the forcing region. This includes the small section directly below the forcing, as well as the aft portion of the data surface that covers the cove. Because forcing contributes directly to acoustic radiation, we should not be surprised that the far-field acoustics includes a significant contribution from the forcing.

Recall that the spectrum obtained using the on-body data surface (Fig. 12) showed a significant decrease in acoustic energy at frequencies below 10,000 Hz. In retrospect, use of the zero-velocity condition on the entire slat surface was incorrect; forcing prescribes

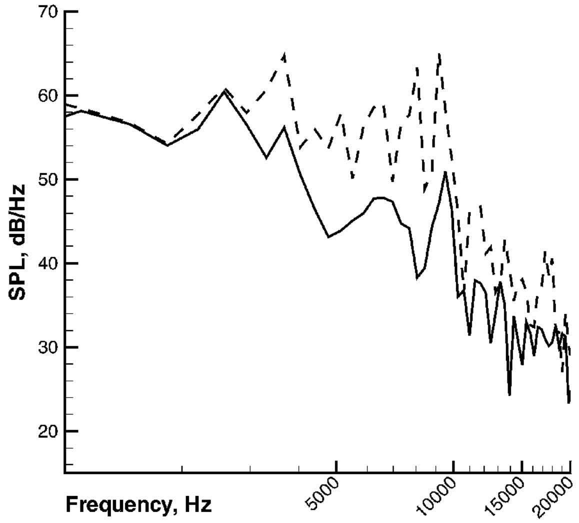

Fig. 14 Far-field noise spectra at 270 deg for 3% forcing $700 < f < 10{,}000$ Hz: ——, modified off-body data surface and - - -, standard off-body data surface, with reference pressure 20 μPa.

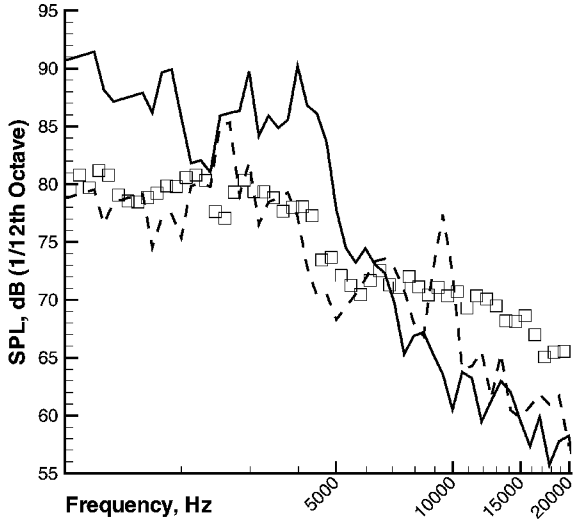

Fig. 15 Far-field noise spectra at 270 deg with modified off-body data surface with ——, 3% forcing $1200 < f < 5000$ Hz; - - -, 3% forcing $700 < f < 10{,}000$ Hz; and □, SPL data $\frac{1}{12}$th octave with reference pressure 20 μPa.

flow through the surface. The on-body data surface with zero surface velocity effectively filtered out much of the noise that would have been radiated directly from the forcing. Because the term L_i on the right-hand side of Eq. (3) is still nonzero, even with zero surface velocity the entire direct noise radiation from forcing is not removed.

To estimate what the acoustic radiation would be without forcing, we constructed the modified data surface shown in Fig. 5c. It consists of the on-body data surface portion over the slat suction surface and the off-body data surface elsewhere. This modified data surface removes a portion of the direct acoustic radiation attributable to forcing and, therefore, provides a better representation of the acoustic radiation expected for a slat–cove shear layer excited by natural perturbations in the flow. The acoustic spectrum for the case with 3% forcing from 700 to 10,000 Hz using the modified off-body data surface is compared with the results derived from using the standard off-body data surface (Fig. 14). A significant decrease in acoustic energy occurs at frequencies between 4000 and 10,000 Hz.

Figure 15 compares the SPLs from the numerical simulations with experimental data. Because the experimental SPL was available only in $\frac{1}{12}$th octave, corresponding results from the numerical simulations have been transformed to $\frac{1}{12}$th octave. Although the experimental data appear to agree well with the computational results, a lack of perfect coherence in the spanwise direction in the experiment should have led to the two-dimensional calculations overpredicting the noise. As elaborated in the preceding section, lack of a proper amplitude may be attributed to premature dissipation of the large-scale structures. Although a smaller discrepancy would have been desirable, the important point is that the decrease in SPL occurs at approximately the same frequency in both the experiment and the simulation. This suggests that numerical simulations are capturing the basic physical mechanisms responsible for the noise.

Conclusions

Time-accurate RANS simulations on a fine grid were used to identify the sources of flow unsteadiness in a slat's cove region. Formation and subsequent development of the free shear layer near the cusp was captured. Initial computations were conducted without forcing. These calculations suggested that the shear layer supports low-frequency oscillations. To better isolate the unsteady mechanism (s), subsequent simulations involved forcing of the shear layer on the slat surface near the cusp. Simulations obtained with narrow-frequency and wide-frequency excitation bands produced nearly identical final states. Analysis of the computational database revealed the shear layer underwent and maintained large-scale flow oscillations. Amplification of the initial forcing field was achieved via the Kelvin–Helmholtz (inflectional) instability mechanism, resulting in the shear layer rollup process and formation of discrete vortices. The amplified disturbances resided in the frequency band $1000 < f < 4000$ Hz, corresponding to the band of frequencies with large amplitudes in the slat's acoustic spectra. Once formed, the discrete vortices underwent severe distortion as they approached the shear layer reattachment point on the slat underside surface. Beyond the reattachment point, the vortices disintegrated and virtually disappeared before reaching the slat trailing edge. For the angle of attack considered, no vortex was observed to escape through the slat gap.

The far-field noise was computed by solving the FW–H equation with a permeable data surface. Flow from the unsteady RANS calculations was used to provide the necessary information on the data surface. Only the surface terms were included in the computation. Preliminary computations of the acoustic field suggested that the imposed forcing used to excite the instabilities dominated the acoustic field. Additional calculations, using a variety of data surfaces, revealed that direct acoustic radiation associated with the imposed forcing accounted for much of the observed noise. A significant portion of the direct radiation was eliminated by use of a data surface that coincided with the slat body in the region of imposed forcing. The resultant acoustic spectrum has a broad peak in the 3000-Hz range, similar to what is seen in the experimental data. Although the amplitude of the computed noise is less than expected, the spectrum shape in the midfrequency range is similar to that measured. This similarity suggests that growth of vortices in the shear layer is possibly responsible for radiated noise in this frequency range.

Acknowledgments

Work of the first and third authors was partially sponsored by NASA Contract NAS1-20102 (Lockheed Martin Corp. Subcontract RT46324) while they were working at High Technology Corp. The majority of the simulations were performed on the C-90 Cray computers provided by the National Aerodynamic Simulation Facility. The authors have greatly benefited from interactions with members of the Airframe Noise Team at NASA Langley Research Center. In particular, many useful discussions with Meelan Choudhari, Craig Streett, and David Lockard are gratefully acknowledged.

References

[1] Macaraeg, M. G., "Fundamental Investigations of Airframe Noise," AIAA Paper 98-2224, 1998.

[2] Hayes, J. A., Horne, W. C., Soderman, P. T., and Bent, P. H., "Airframe Noise Characteristics of a 4.7% Scale DC-10 Model," AIAA Paper 97-1594, 1997.

[3] Dobrzynski, W., Nagakura, K., Gehlhar, B., and Buschbaum, A., "Airframe Noise Studies on Wings with Deployed High-Lift Devices," AIAA Paper 98-2337, June 1998.

[4] Davy, R., and Remy, H., "Airframe Noise Characteristics on a 1/11 Scale Airbus Model," AIAA Paper 98-2335, June 1998.

[5] Grosche, F.-R., Schneider, G., and Stiewitt, H., "Wind Tunnel Experiments on Airframe Noise Sources of Transport Aircraft," AIAA Paper 97-1642, 1997.

[6] Michel, U., Barsikow, B., Helbig, J., Hellmig, M., and Schuttpelz, M., "Flyover Noise Measurements on Landing Aircraft with a Microphone Array," AIAA Paper 98-2336, 1998.

[7] Storms, B. L., Hayes, J. A., Moriarty, P. J., and Ross, J. C., "Aeroacoustic Measurements of Slat Noise on a Three-Dimensional High-Lift System," AIAA Paper 99-1957, 1999.

[8] Olson, S., Thomas, F. O., and Nelson, R. C., "Preliminary Investigation into Slat Noise Production Mechanisms in a High-Lift Configuration," AIAA Paper 2000-4508, 2000.

[9] Khorrami, M. R., Berkman, M. E., and Choudhari, M., "Unsteady Flow Computations of a Slat with a Blunt Trailing Edge," *AIAA Journal*, Vol. 38, No. 11, 2000, pp. 2050–2058.

[10] Singer, B. A., Lockard, D. L., and Brentner, K. S., "Computational Acoustic Analysis of Slat Trailing-Edge Flow," *AIAA Journal*, Vol. 38, No. 9, 2000, pp. 1558–1564.

[11] Paschal, K., Jenkins, L., and Yao, C., "Unsteady Slat Wake Characteristics of a Two-Dimensional High-Lift Configuration," AIAA Paper 2000-0139, 2000.

[12] Takeda, K., Ashcroft, G. B., and Zhang, X., "Unsteady Aerodynamics of Slat Cove Flow in a High-Lift Device Configuration," AIAA Paper 2001-0706, 2001.

[13] Menter, F., "Improved Two-Equation k–ω Turbulence Models for Aerodynamic Flows," NASA TM 103975, 1992.

[14] Rumsey, C. L., Sanetrik, M. D., Biedron, R. T., Melson, N. D., and Parlette, E. B., "Efficiency and Accuracy of Time-Accurate Turbulent Navier–Stokes Computations," *Computers and Fluids*, Vol. 25, No. 2, 1996, pp. 217–236.

[15] Singer, B. A., Brentner, K. S., Lockard, D. L., and Lilley, G. M., "Simulation of Acoustic Scattering from a Trailing Edge," *Journal of Sound and Vibration*, Vol. 230, No. 3, 2000, pp. 541–560.

[16] Ffowcs Williams, J. E., and Hawkings, D. L., "Sound Generated by Turbulence and Surfaces in Arbitrary Motion," *Philosophical Transactions of the Royal Society*, Vol. A264, No. 1151, 1969, pp. 321–342.

[17] Brentner, K. S., and Farassat, F., "An Analytical Comparison of the Acoustic Analogy and Kirchhoff Formulation for Moving Surfaces," *AIAA Journal*, Vol. 36, No. 8, 1998, pp. 1379–1386.

[18] Lockard, D. P., "An Efficient, Two-Dimensional Implementation of the Ffowcs-Williams and Hawkings Equation," *Journal of Sound and Vibration*, Vol. 229, No. 4, 2000, pp. 897–911.

P. J. Morris
Associate Editor